Environmental Science Nano

ROYAL SOCIETY OF CHEMISTRY

PAPER

View Article Online
View Journal | View Issue

Cite this: *Environ. Sci.: Nano*, 2021, **8**, 342

Bi_2O_3/nylon multilayered nanocomposite membrane for the photocatalytic inactivation of waterborne pathogens and degradation of mixed organic pollutants†

Tanveer A. Gadhi, [a] Aizaz Qureshi,[a] Najeebullah Channa,[a] Rasool Bux Mahar,[a] Alessandro Chiadò, *[b] Chiara Novara[b] and Alberto Tagliaferro [b]

Received 14th October 2020,
Accepted 16th December 2020

DOI: 10.1039/d0en01026j

rsc.li/es-nano

A powder semiconductor α/β-Bi_2O_3 was synthesized *via* solid state thermal annealing and further composited with a multilayered nylon fibrous membrane *via* electrospraying. The successful integration of nano-sized α/β-Bi_2O_3 into the nylon membrane was confirmed by XRD, FESEM images, UV-vis, FT-IR and Raman analyses. The nanocomposite membrane displayed a visible light-responsive catalytic ability with an energy bandgap of 2.78 eV estimated from the data of DRS. The activity of the composite membrane was examined in a continuous mode reactor for the degradation of separate and mixed solutions of anionic (indigo carmine) and cationic (rhodamine B) organic pollutants. Moreover, the composite membrane exhibited antibacterial properties towards *E. coli*, a waterborne pathogen, as revealed by the obtained growth inhibition during the Kirby–Bauer and liquid culture tests. The inactivation of *E. coli* was confirmed by live/dead cell staining using fluorescence imaging. Finally, a mixed solution of organic dyes at different concentration, as well as the recycle of the membrane, showed the stability and potential of the α/β-Bi_2O_3 composite membrane for the removal of organic pollutants and inactivation of the waterborne pathogen.

Environmental significance

Worldwide, there is an increasing demand for clean water and sanitation systems and different solutions are under evaluation, including advanced oxidation processes such as photocatalysis. This work describes the scalable synthesis process of an electrospun composite membrane made of nylon and embedded α/β-Bi_2O_3 nanoparticles that can be activated by visible light instead of UV light typically used with other nanomaterials (*e.g.* TiO_2). As a proof of concept, the efficacy of the α/β-Bi_2O_3 electrospun composite membrane in the visible light inactivation of pollutants and pathogens was demonstrated in a continuous-flow photocatalytic membrane reactor, highlighting the great potential of this advanced photocatalytic process for clean water and sanitation.

1. Introduction

Nowadays, there is an increasing demand for clean water and sanitation. One of the emerging technologies to get sustainable clean water can be based on advanced oxidation processes (AOPs). Among them, heterogeneous photocatalysis is an AOP in which semiconductor materials are illuminated with solar/UV light to facilitate redox reactions and enable the treatment of organic, inorganic species, and microbes.[1,2] However, its suitability in real applications is still challenged by various essential aspects. One of these is the cost-effective recovery of dispersed particles, their filtration and recycling.[3–5] Indeed, for high photoactivity, nano-scale particles are preferred because of their prominent surface area, better dispersion in bulk reactors, and optimum activation from the irradiation source.[6,7] However, these particles are hard to recover and reuse; moreover, they increase the operational cost of water treatment.[3,4] Alternatively, various studies have suggested diverse materials as fixed supports for the active particles, with a focus on carbon, silica, and mineral-based porous supports that could allow a good contact between the immobilized semiconductors and the targeted contaminant for continuous treatment. Examples of such supports are silica-based,[8–10] activated carbon,[11,12] synthetic clay LAPONITE®,[13] glass, steel mesh,[14–16] and recently some polymers such as polyimide.[17] However, with such immobilized fixed supports, the

[a] *U.S. Pakistan Center for Advanced Studies in Water (USPCASW), Mehran University of Engineering and Technology, Jamshoro 76062, Pakistan*
[b] *Department of Applied Science and Technology, Politecnico di Torino, Corso Duca degli Abruzzi 24, 10129 Torino, Italy. E-mail: alessandro.chiado@polito.it*
† Electronic supplementary information (ESI) available. See DOI: 10.1039/d0en01026j

photocatalytic response is reportedly lower than using bulk materials, because of low dispersion, reduced transparency, limited mass transfer, and weak interaction of the immobilized semiconductor with the targeted contaminants.[3] Thus, these limitations hinder the advancement of non-slurry application alternatives, as the immobilization supports should satisfy requirements of chemical inertness, transparency to the irradiation source, and adequate channels and permeation to capture the targeted contaminants in bulk reactors.[18,19]

Merging membrane and photocatalytic technologies has been considered recently. In this case, the semiconductor materials could be incorporated/embedded within the porous membrane to maximize the degradation efficiency. Such an approach turned into a great achievement in treating wastewater. The porous network of tiny channels in the membrane could be used to embed the semiconductor materials, and further to capture and adsorb the contaminants, so that their removal could be maximized. Recent results have shown that adding semiconductor particles to the membrane has improved water flux,[20] refined permeability and selectivity,[21] boosted antifouling properties[22] and increased adsorption sites, which ultimately enhanced the adsorption of the membrane.[23] Different kinds of materials were used to prepare photocatalytic membranes such as ceramics, zeolites, but mostly polymers.[24] However, irradiation and generation of oxidizing species in the reaction environment cause abrasion and leaching of the semiconductor from the membrane itself.[24] Therefore, for its chemical, thermal, and mechanical stability, nylon polymer could be a promising option for semiconductor embedding and composite usage as a photocatalytic membrane. Indeed, electrospun nylon-6 nanofibers have a large surface area and active sites that could improve the adsorption of pollutants for the subsequent degradation.[25] Moreover, the electrospun nanofibers have demonstrated improved properties in dye removal,[26] advanced filtration,[27] and antibacterial applications.[28]

Besides the degradation and removal of organic and inorganic pollutants, various studies have explored the potential of semiconductor–polymeric composite membranes for the inactivation and removal of pathogens through the same principle *i.e.* the attack of the cell membrane through reduction–oxidation reactions and consequently reduction in their growth.[28,29] Some of the reported semiconductor composite membranes include embedded oxides of silver, titanium, cerium, zirconium, and iron, and have shown antimicrobial response against common pathogens *i.e.* *Escherichia coli*, *Staphylococcus aureus*, *Enterococcus* sp., *Pseudomonas aeruginosa*, and *Klebsiella pneumonia*.[30–33] Amongst various semiconductors, bismuth-based materials, such as $BiVO_4$,[34] Bi_2O_3,[35,36] BiOX (Cl, I, Br),[37] and bismuth-based composites,[38,39] have been proven efficient in water treatment due to their ability to produce reactive oxygen species (ROS). Among them, Bi_2O_3 has emerged as the most effective visible light-responsive material with promising optical, electrical, thermal, and photocatalytic properties.[40] Moreover, it also has a tunable bandgap between 2.1 and 2.8 eV compared to 3.2 eV of TiO_2. The solar light viable bandgap is a result of the Bi_2O_3 hybrid valence band arising from contributions of Bi 6s and O 2p orbitals; in contrast, the TiO_2 valence band only has O 2p orbital contributions.[41]

To the best of our knowledge, Bi_2O_3–polymeric nanocomposite membranes have rarely been investigated against the removal of both organic pollutants and waterborne pathogens. Therefore, this study was conducted to exploit and investigate the potential of Bi_2O_3 integration into a nylon-6 membrane. Once synthesized, the membranes were characterized by XRD, FESEM, UV-vis, FT-IR and Raman analyses, to check the proper integration of the α/β-Bi_2O_3 nanomaterials into the nylon membrane. Afterward, the degradation efficiency of the composite membranes against single and mixed solutions of anionic (indigo carmine) and cationic (rhodamine-B) organic dye pollutants and against a pathogenic strain of *E. coli* was evaluated by using a continuous-flow photocatalytic membrane reactor (CPMR), paving the way for a new approach in achieving water purification.

2. Experimental section

2.1 Materials and chemicals

Nylon-6 pellets (density of 1.084 g mL^{-1}), formic acid, ethanol, polyethylene glycol (PEG), Triton-X, bismuth(III) nitrate pentahydrate ($Bi(NO_3)_3{\cdot}5H_2O$), indigo carmine (IC), and rhodamine B (RhB) were purchased from Sigma Aldrich, Italy. Sodium chloride (NaCl) was purchased from Daejung Co. Ltd., Korea. The bacterial culture media (agars and broths) were purchased from Oxoid, England. For live/dead cell staining, a LIVE/DEAD® BacLight™ Bacterial Viability kit was purchased from ThermoFisher Scientific, USA; this kit included two staining dyes, SYTO-9 and propidium iodide (PI), at 20 mM concentration each. All the materials and chemicals were used as received.

2.2 Synthesis of α/β-Bi_2O_3

The α/β-Bi_2O_3 powder was synthesized from $Bi(NO_3)_3{\cdot}5H_2O$ by solid state thermal annealing route. The synthesis details are published elsewhere.[42] In brief, the measured quantity of $Bi(NO_3)_3{\cdot}5H_2O$ was placed in a ceramic crucible and directly heated inside a muffle furnace at an initial temperature of 150 °C for 30 min. Afterward, the temperature was raised to 250 °C and kept constant for 2 h, and finally, the temperature was increased to 550 °C for 45 minutes to obtain the α/β-Bi_2O_3 composite. This composite (in bulk form) was already reported as a visible light-responsive semiconductor for the degradation of organic compounds.[42]

2.3 Preparation of the Bi_2O_3/nylon composite membrane

The obtained α/β-Bi_2O_3 powder (10 wt%) was dissolved in ethanol. Measured drops of PEG and Triton-X were gradually added into the ethanol mixture under continuous mixing *i.e.* to ensure a well-segregated particle suspension and

homogenization. The obtained solution was stirred for 18 hours and then sonicated for 30 minutes to get a homogeneous yellow colored solution. The nylon-6 solution was made by dissolving 22 wt% nylon pellets in formic acid, stirring it continuously at 100 rpm for 6 hours to produce a neat and transparent nylon-6 solution. Then, the nylon-6 solution was electrospun to produce a multilayered nylon fibrous membrane. The multilayers referred to the electrospun and stacked fibrous layers of nylon that overlaid one after another. The applied voltage was altered between 18 and 24 kV to obtain thick and ultra-thin spiderweb type multilayered nano-fibers.[43] The injection flow rate was set to 0.95 mL h^{-1} at a 12 cm tip to collector distance. Electrospinning was followed by electrospray of the α/β-Bi_2O_3 solution on the surface of the obtained nylon electrospun multilayers *i.e.* for successful integration of α/β-Bi_2O_3. Fig. 1 depicts the scheme of the electrospinning process for the preparation of bare and α/β-Bi_2O_3 composite membranes and the digital image of the obtained membrane. The obtained membranes were referred to as bare-nylon and Bi_2O_3/nylon composite. Visually, the surface of the obtained Bi_2O_3/nylon membrane showed a homogeneous pale-yellow non-dusty appearance as an indication of the embedded Bi_2O_3 particles.

2.4 Characterization of the bare and composite membranes

To observe and analyze the microstructure and morphology of the obtained bare and composite membranes, an in-lens detector of a Zeiss Supra 40 field emission scanning electron microscope (FESEM) was used to acquire secondary electron contrast images with 5 keV electrons (Zeiss SMT, Oberkochen, Germany). Energy-dispersive X-ray spectroscopy (EDX) analysis was performed during FESEM imaging. To this aim, all the peaks were used for the elemental analysis (3 iterations), which was carried out with 15 keV electrons. To analyze the size and phase composition of the obtained membranes, a Panalytical X'Pert MRD Pro Cu Kα X-ray source in Bragg/Brentano configuration was used. The sample was scanned in a 2θ range of 20–60°. A Varian Cary 500 spectrophotometer equipped with an integration sphere was used to record the diffuse reflectance spectroscopy (DRS) and transmittance spectra of the bare and composite membranes. Tauc plots of the Kubelka–Munk function were used to calculate the energy bandgap (E_g) value. FT-IR analysis was performed in attenuated total reflection (ATR) mode to identify the chemical changes in the membrane after the incorporation of α/β-Bi_2O_3. The spectra were collected with a 4 cm^{-1} resolution by accumulating 64 scans each spectrum on a Nicolet 5700 FTIR spectrometer (Thermo Fisher) equipped with a diamond crystal and a DTGS detector (at room temperature) in the 400–4000 cm^{-1} range. Raman spectra were acquired with a 785 nm laser source using an InVia Qontor Raman microscope (Renishaw plc, Wotton-under-Edge, UK) equipped with a 20× objective, in backscattering configuration. The output laser power was attenuated to 25 mW and the acquisition time was 50 s.

2.5 Photocatalytic evaluation

2.5.1 Continuous-flow photocatalytic membrane reactor (CPMR). Fig. 1 shows the schematic diagram of the in-house fabricated CPMR for the evaluation of the efficacy of the membranes on selected dyes and bacteria. The CPMR includes a cylindrical tube made of borosilicate glass with four membrane holders (each 6 × 6 cm) for placing the prepared membrane in a straight position at a distance of 10 cm from each other. A white LED light source for the activation of integrated α/β-Bi_2O_3, with a measured irradiance of around 70 W m^{-2} (at the cylinder's center of all positioned membranes) and an emission spectrum between 400 and 700 nm, was attached outside of the cylinder. Beneath the cylindrical tube, the storage tank was connected *via* a

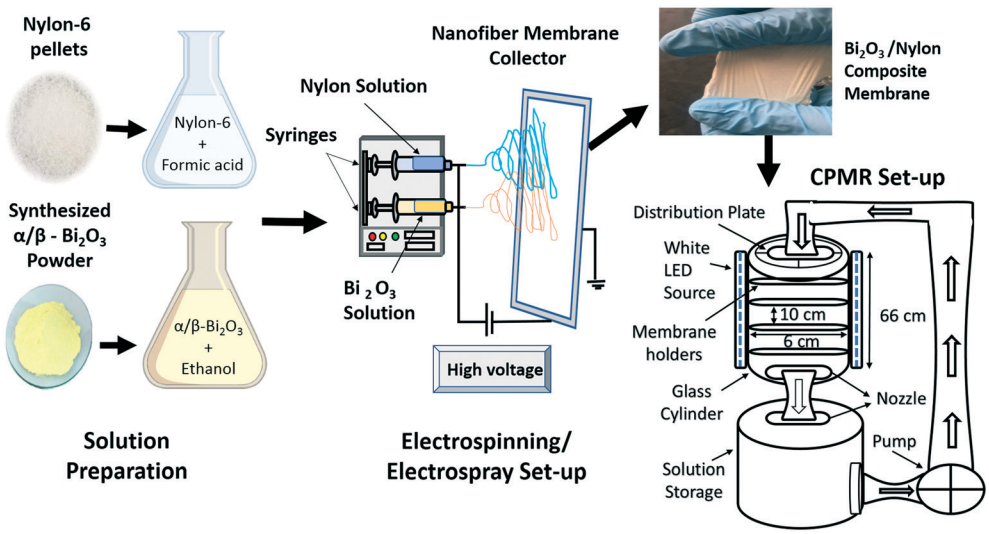

Fig. 1 Schematic layout of membrane preparation and photocatalytic tests.

peristaltic pump *i.e.* for the circulation of the stock solution (2 L) over the membrane (*i.e.* inside the cylindrical tube) at a constant flow of 25 mL min^{-1}. For dark conditions, the LED light remained switched-off; besides, aluminum foil was wrapped on the cylindrical tube.

2.5.2 Photocatalytic discoloration tests. Anionic IC and cationic RhB dyes were selected as model pollutants because of their common use in photocatalytic evaluation.[42] For the preliminary experiments, both dyes were tested separately at a concentration of 5 ppm. Initially, to achieve adsorption/desorption equilibrium, the LED light remained switched-off for the first 30 minutes. Afterward, the solution was irradiated to analyze the photocatalytic removal and assess the degradation kinetics. 3 mL of the samples was collected in a predefined time sequence of photocatalytic treatment, centrifuged for 5 minutes for the analysis, and afterward returned to the stock solution to avoid any interference with the system kinetics. The centrifuged samples were analyzed using a double beam UV-vis spectrophotometer (Perkin Elmer-LAMBDA 365) for recording the time-dependent intensity reduction and changes in the absorbance spectra of the model pollutants. For the mineralization degree of the treated dye solutions, total organic carbon (TOC) analysis was carried using a TOC-L SHIMADZU TOC analyzer. For TOC analysis, the control and the treated samples of both dyes were collected and analyzed using a protocol reported in the literature.[44] The stability of the membrane was evaluated by testing the same membrane up to three cycles using the IC solution at a fixed concentration of 5 ppm. Before reuse, the recovered membranes were thoroughly rinsed with distilled water.

For the composite membrane performance against the mixed regime of dyes, *i.e.* of different chemical structures and ionic behaviors, separately prepared solutions of IC and RhB (at a molar concentration of 1×10^{-6} M) were mixed at even proportions. The prepared mixed stock of 2 L was evaluated in the CPMR, under similar operating conditions, as mentioned earlier.

2.5.3 Photocatalytic bacterial inhibition/inactivation. Initially, the inhibition of *E. coli* ATCC (8739) was performed on agar plates, using the bare and composite membranes cut into 10 × 10 mm^2 pieces. In brief, the inoculum (100 μL) was taken from the overnight incubated *E. coli* culture at a concentration of 1×10^6 CFU mL^{-1} and was spread on LB agar plates. Then, the bare nylon/composite membrane was placed at the center of the plate and incubated for 24 h at 37 ± 1 °C; the test was performed in the dark or in the presence of a white LED lamp (100 W m^{-2}). After 24 hours, the inhibition zone was observed in the culture plates.[45] The experiments were conducted in duplicate, and the zone of inhibition was calculated as suggested in previously reported studies.[46,47] Further, for the evaluation of the liquid bacterial suspension, *E. coli* was inoculated in a 50 mL tube of LB broth (Oxoid, England) after overnight incubation at 37 °C and shaking at 120 rpm. Afterward, the culture broth was centrifuged at 5000 rpm for 10 minutes, and the settled pellets were washed several times with a sterilized normal saline solution (0.85% of NaCl). Then, the bacterial biomass was diluted in 2 L of saline solution to reach a bacterial concentration of around 1×10^6 CFU mL^{-1}, by measuring an optical density (OD) of 0.01 at 600 nm. The prepared bacterial stock was tested in the CPMR for photocatalytic inactivation, at 25 mL min^{-1}. Initially, the dark conditions were maintained for 30 minutes, then the cylindrical tube was irradiated. A 100 μL sample was collected in a predefined time sequence of photocatalytic treatment. The collected samples were serially diluted and plated on LB agar plates, incubated for 24 hours at 37 °C, and the numbers of bacterial colonies were counted.

To observe if the photocatalytic action was able to damage the *E. coli* cells, live/dead bacterial cell fluorescence staining was performed. For this, a 1 mL sample was collected at different time intervals, centrifuged at 10 000 rpm for 15 minutes, and then the bacterial biomass was washed with sterilized saline solution. Finally, the obtained bacterial biomass was resuspended in 1 mL of sterilized saline solution. Afterward, by following the protocol provided in the received live/dead fluorescence staining kit, a 1 : 1 mixed dye stock solution of SYTO-9 (3.34 mM, excitation 483 nm, emission 503 nm) and propidium iodide (PI; 20 mM, excitation 535 nm, emission 617 nm) was prepared. For fluorescence microscopy imaging, 5 μL of the mixed dye stock solution was added into the bacterial suspension and incubated in the dark for 30 minutes. After incubation, 5 μL of the stained bacterial suspension was collected and pipetted over a glass slide and covered for fluorescence analysis. A fluorescence microscope (Zeiss Axio Scope.A1, Carl Zeiss, Germany) equipped with FITC and Texas RED filters was used to acquire fluorescence images. The acquired images were analyzed *via* ImageJ 1.50d to assess the percentage of live (green-stained) and dead (red-stained) bacterial cells.

3. Results and discussion

3.1 Characterization

The composite membrane containing the bismuth oxide-based nanomaterial was synthesized and characterized, as described in the experimental part. In the following, the physical–chemical characterization using XRD, UV-vis, FT-IR, Raman spectroscopy, FESEM imaging, EDX analysis is reported.

3.1.1 XRD analysis. The XRD patterns of bare nylon, Bi_2O_3/nylon, and synthesized α/β-Bi_2O_3 powder are shown in Fig. 2A. The bare nylon, being semi-crystalline, does not show any peak, while in the case of the Bi_2O_3/nylon composite some peaks were observed at 27.06°, 31.7°, and 53.6°, indicating the formation of the monoclinic α-Bi_2O_3 phase.[42] These peaks match with standard XRD data (JCPDS 16-0654).[43] Additional peaks were observed at 2θ = 27.96, 32.72°, and 46.22°, corresponding to the β-Bi_2O_3 phase (JCPDS card no. 01-078-1793).[42] As shown by the comparison in Fig. 2A, the pattern of the Bi_2O_3/nylon composite retained the main peaks observed for the α/β-Bi_2O_3 powder after integration into nylon by electrospinning. However, due to the dilution

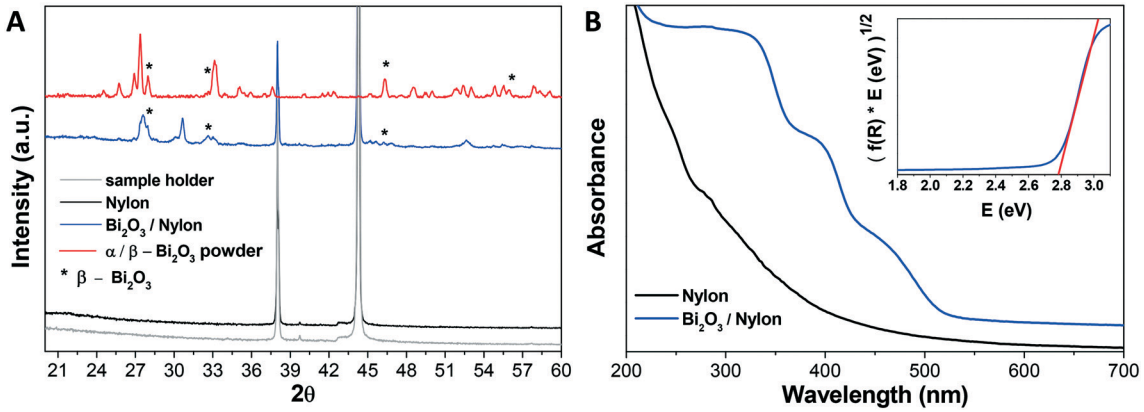

Fig. 2 A) XRD patterns of the sample holder, bare nylon, Bi_2O_3/nylon composite, and synthesized α/β-Bi_2O_3 powder, and B) UV-vis DRS spectra of bare nylon and Bi_2O_3/nylon composite; inset: Tauc plot for the estimation of the bandgap.

in the nylon membrane, the weaker peaks in the XRD spectra of α/β-Bi_2O_3 could not be detected.[48]

3.1.2 Optical properties. Fig. 2B shows the DRS spectra of the bare and composite nylon membranes. The bare nylon displayed a slight absorption in the region 250 nm to 300 nm, typical of nylon polymer.[49] Meanwhile, the Bi_2O_3/nylon composite membrane exhibited one absorbance stretch in the plateau between 375 nm and 450 nm, which is the characteristic optical transition range of α-Bi_2O_3. Moreover, the extended absorbance stretch in the range of 450–530 nm represented the characteristic transition range of β-Bi_2O_3.[42] The observed absorption edge in the visible spectrum could facilitate the transition of the electrons from the valence to the conduction band and consequently allow the composite membrane to harvest solar irradiation for photocatalytic activity.[34] The bandgap of the composite membrane estimated from the Tauc plot was around 2.78 eV, *i.e.* shown in the inset of Fig. 2B. As per the XRD analysis, the α-phase is dominant in the α/β-Bi_2O_3 composite. Therefore, the two absorption edges in the visible region have a combined representation in the Tauc plot, and the predominant characteristics of α-Bi_2O_3 were slightly narrowed due to the presence of β-Bi_2O_3.

3.1.3 FESEM analysis. Fig. 3 shows the FESEM images of bare nylon (Fig. 3A and B) and the Bi_2O_3/nylon composite (Fig. 3C and D) at different magnifications. In the case of bare nylon, the images exhibit both thick and thin electrospun nanofiber strands in the range of 20–60 nm diameter that form a net-like structure with overlaid multilayers.[43,50] The obtained nanofibers displayed a uniform and bead-free formation. In the case of the Bi_2O_3/nylon composite, the FESEM image in Fig. 3C shows the integration of nano-sized round Bi_2O_3 particles into the nylon fibers. Moreover, Fig. 3D suggests that this integration was achieved across each electrospun layer and in the whole thickness of the membrane.

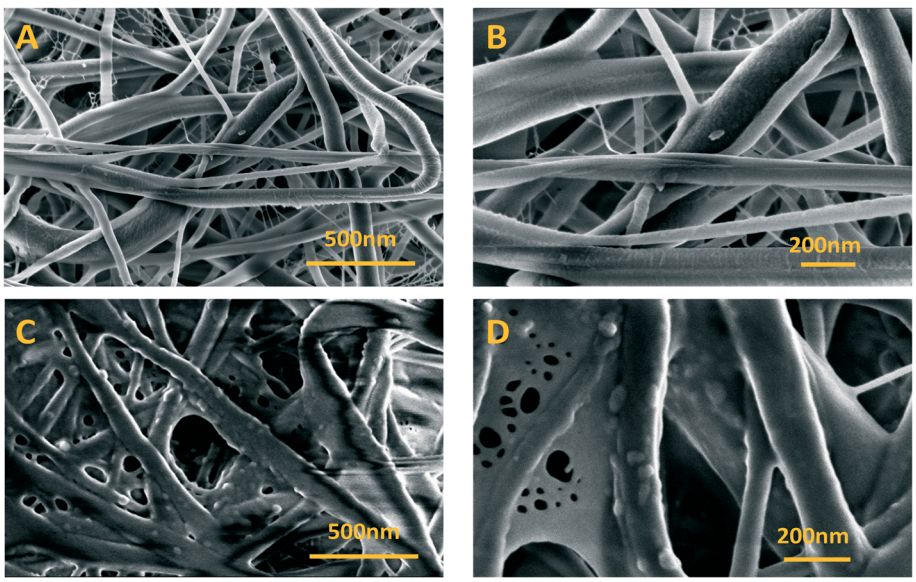

Fig. 3 FESEM images of bare nylon and Bi_2O_3/nylon membranes at different magnifications. (A) Bare nylon (25k×), (B) (50k×), (C) Bi_2O_3/nylon (25k×), and (D) (50k×).

A further confirmation of the integration of the bismuth nanomaterial into the multilayered electrospun membrane was revealed by EDX analysis, reported in Fig. S1.† This evaluation clearly revealed the presence of Bi atoms in the Bi_2O_3/nylon membrane.

3.1.4 FT-IR analysis. Fig. 4 shows the FT-IR spectra of the bare and composite membrane samples. Nylon-6 is a polyamide; therefore, its molecular structure is characterized by the presence of amide groups as displayed by the amide I stretching at 1638 cm^{-1} (C═O stretching) and amide II stretching at 1540 cm^{-1} (as a combination of –CN stretching and –NH bending).[51] At the same time, the intense band at 3297 cm^{-1} indicates the N–H stretching vibration.[52] The peaks at about 1367 cm^{-1}, 1263 cm^{-1}, and 1200 cm^{-1} are due to amide III stretching and CH_2 wagging, while the peaks at 2860 cm^{-1} and 2933 cm^{-1} are due to CH_2 symmetric and asymmetric stretching, respectively.[52] All other peaks match with FT-IR assignments of nylon-6 nanofibers reported previously and summarized in Table S1.†[51,52] In the Bi_2O_3/nylon composite, concerning Bi_2O_3, its leading bands are below 500 cm^{-1}, but the ATR diamond crystal used to acquire the spectra cuts this region. The only clear signal of bismuth oxide is the peak at 846 cm^{-1} due to the symmetric Bi–O stretching.[53] Nevertheless, some of the absorption bands of nylon-6 are downshifted. In particular, the amide I and amide II bands are shifted to 1635 cm^{-1} and 1538 cm^{-1}, respectively, whereas the N–H stretching is shifted to 3294 cm^{-1}. This is probably the result of the interaction of the nylon polymer with Bi_2O_3.

3.1.5 Raman analysis. Raman analysis of the bare nylon and composite membranes was performed to further assess the incorporation of the α/β-Bi_2O_3 nanoparticles. As shown in Fig. 5 the nylon fibers are characterized by a weak Raman signal that matches the typical vibrational pattern of polyamides.

In detail, different bands assigned to CC stretching coupled to CH_2 bending modes are observed around 1100 cm^{-1} (CC stretching + CH_2 twisting around 1080 cm^{-1} and CC stretching + CH_2 wagging at 1120 cm^{-1}), while two CH_2 twisting bands and one CH_2 bending-related band are detected between 1260 and 1300 cm^{-1} and at 1440 cm^{-1}, respectively.[54] Finally, the amide I band appears at about 1635 cm^{-1}.[55] The addition of the Bi_2O_3 nanopowder results in significant changes in the low Raman shift range, while the vibrational pattern is almost unaffected over 600 cm^{-1}, except for a narrow band at 1040 cm^{-1} due to residual nitrates from the synthesis. The emergence of intense Raman modes in the 120–600 cm^{-1} range, attributable to two different Bi_2O_3 crystalline phases, clearly evidences the incorporation of the bismuth oxide in the membrane. The bands at 278, 313 and 440 cm^{-1} were previously assigned to α-Bi_2O_3.[56,57] Meanwhile, the vibrational modes at 142 and 335 cm^{-1} appear slightly up-shifted with respect to the main bands of β-Bi_2O_3 (128 cm^{-1} and 317 cm^{-1}),[58] but can still be consistent with the presence of the

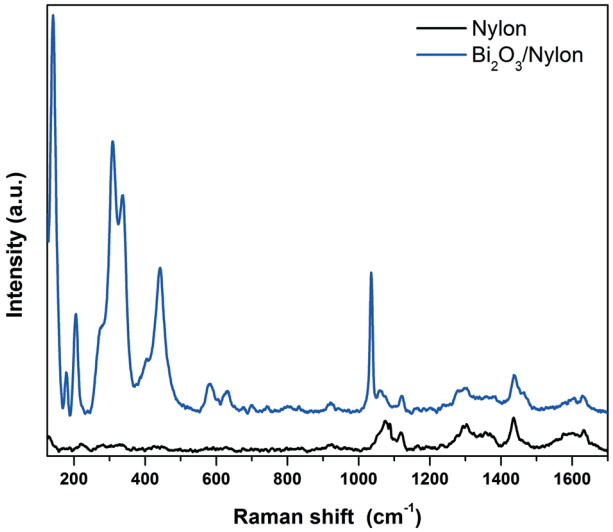

Fig. 5 Raman spectra of the bare (bottom black curve) and α/β-Bi_2O_3 decorated (top blue curve) nylon membranes.

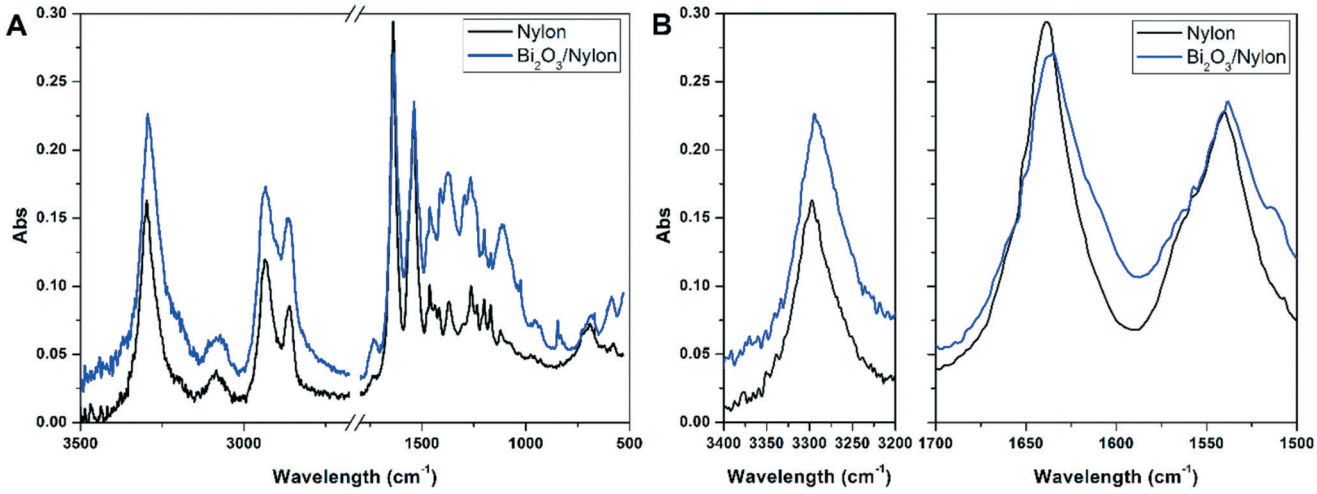

Fig. 4 FT-IR patterns of nylon and Bi_2O_3/nylon membranes: A) whole FT-IR spectrum; B) magnification of the N–H stretching (left) and amide I and amide II (right) regions.

tetragonal phase. Depending on the Raman shift region where they occur, the observed Raman bands can be attributed to Bi-dominated lattice movements (<155 cm^{-1}), modes with significant Bi and O contributions (155–255 cm^{-1}) and oxygen related displacements (>255 cm^{-1}), as derived previously for α-Bi_2O_3.[57] Raman analysis thus confirms both the formation of the composite and the preservation of the crystalline phases of the nanopowder after electrospinning.

3.2 Photocatalytic dye discoloration/degradation

Once the composite membrane has been physico-chemically characterized, its photocatalytic efficiency was evaluated, employing photocatalytic tests against anionic IC and cationic RhB organic dyes. The selection of these dyes was made to compare the obtained results with previously reported ones, in which both dyes were evaluated individually and in a mixed solution using the bulk α/β-Bi_2O_3 powder.[42]

3.2.1 Indigo carmine (IC) dye. Fig. 6A shows the relative concentration (C/C_o) profile of IC dye at different times of photocatalytic exposure, using bare nylon and Bi_2O_3/nylon composite membranes. The absorption spectra of IC *vs.* different treatment times using Bi_2O_3/nylon are given in Fig. S2 of the ESI.† Initially, under dark conditions, the absorbance of IC at 610 nm was reduced by 21.4% due to its charge interactions with the nylon multilayers.[59] Any further decrease due to adsorption was not observed for a longer period in the dark. Instead, after irradiation exposure, the absorbance peak of IC started to decrease further, due to the photocatalytic response of α/β-Bi_2O_3, until it completely disappeared after prolonged exposure of 180 minutes. The removal of IC is due to the oxidation and breaking of the indigoid group (NHC═CNH), as indicated by the observed isosbestic point at 250 nm and by the increase of absorbance of intermediate products (shown in Fig. S2†) *i.e.* isatin sulfonic acid and 2-amine-5-sulfo-benzoic acid, in the UV absorbance region between 250 nm and 275 nm.[5,42] The persistent appearance of these peaks was probably an indication of incomplete mineralization.[44]

Further, in Fig. 6A the photolysis of IC dye solution, *i.e.* under irradiation exposure without the presence of any membrane, showed no/less significant change in the IC concentration, while in the case of the bare nylon membrane, around 19% of IC dye was initially adsorbed in the dark and,

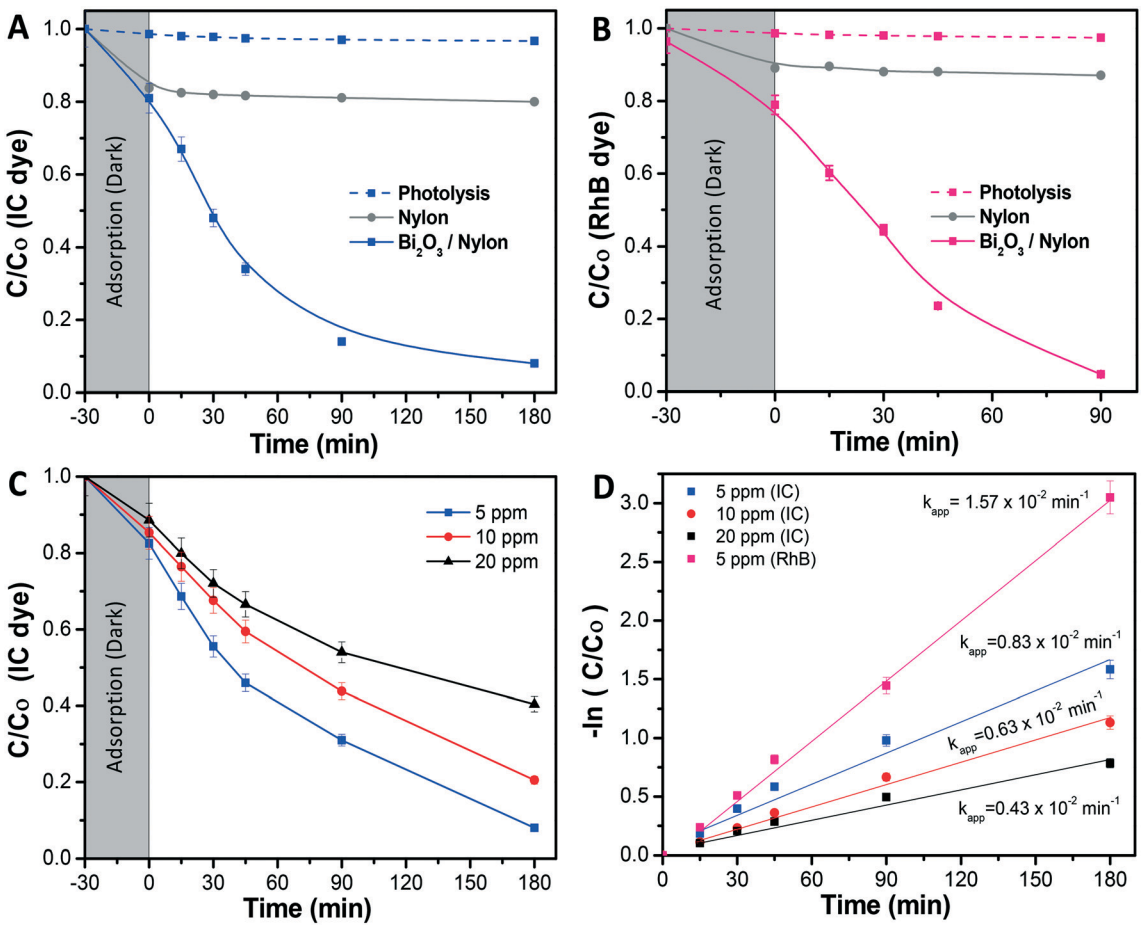

Fig. 6 Photocatalytic tests using bare nylon and Bi_2O_3/nylon composite membranes: A) relative concentration (C/C_o) of IC degradation *vs.* time (C_o = 5 ppm); B) C/C_o of RhB degradation *vs.* time (C_o = 5 ppm); C) C/C_o of different IC dye concentrations with the Bi_2O_3/nylon composite membrane; and D) kinetic curve of IC and RhB dye solutions, and estimated apparent kinetic rates (K_{app}).

afterward, did not show any further activity under light conditions. This could be ascribed to a limited amount of adsorption sites in the nylon fibrous membrane, which could not accommodate further dye molecules, resulting in a limited removal of the dye from the solution.[26] Meanwhile, the Bi_2O_3/nylon composite membrane showed slightly higher adsorption (21.4%), compared to the bare nylon membrane. This could be related to additional adsorption sites provided by the embedded nanoparticles.[23] Afterward, in the following first 45 min of irradiation, the improved removal of IC was observed due to the high concentration of adsorbed IC molecules on the membrane surface, which was rapidly oxidized by the generated ROS after irradiation. Further, after 180 min of irradiation, around 78% of mineralization was achieved, as analyzed by TOC analysis. Afterward, the TOC reduction remained unchanged for a longer run of 360 min, due to the persistent nature of the resulting intermediates.[42] The kinetic curve for the degradation of IC (shown in Fig. 6D; at 5 ppm concentration) is plotted using the $\ln(C_o/C)$ function *vs.* time which resulted in a straight line ascribed to the pseudo-first-order reaction,[44] with a calculated apparent kinetic rate (K_{app}) of 0.83×10^{-2} min^{-1}.

3.2.2 Rhodamine B (RhB) dye. RhB is a cationic dye and has both diethylamine and carboxylic groups.[42] Fig. S3 in the ESI† shows the UV-vis absorbance spectra of RhB at different time intervals obtained with the Bi_2O_3/nylon composite membrane. RhB shows the maximum absorbance peak at 555 nm,[40] which was followed to relate its removal *via* simultaneous adsorption and photocatalytic oxidation. In Fig. 6B, the C/C_o profiles of RhB dye at different times of photocatalytic exposure, using bare nylon and Bi_2O_3/nylon composite membranes, are compared. Initially, 21% of the RhB intensity was reduced due to its interaction with the multilayers and integrated Bi_2O_3 particles *i.e.* under dark conditions, and the adsorption–desorption equilibrium was attained with the saturation of the composite membrane by RhB dye molecules as no further adsorption was noted up to 60 min under dark conditions. The interaction of cationic dyes with nylon is assumed to be weaker than that of anionic dyes. However, an improved interaction of RhB dye with the composite membrane was observed. This could be associated with the anionic carboxylic group of RhB and good protonation of α/β-Bi_2O_3 particles that could have allowed amphoteric sites of RhB to interact with the composite membrane.[42] After irradiation, the adsorbed and highly interacting RhB dye was removed and oxidized by the reactive species generated by the composite α/β-Bi_2O_3 particles after 90 minutes, and reached a degradation and mineralization degree of up to 68% after 180 min of exposure, as observed through TOC analysis. The mineralization of RhB was unchanged after that due to the formation of persistent intermediates.[44] Compared to IC dye, the removal of RhB was found to be faster with a calculated K_{app} of 1.57×10^{-2} min^{-1} *i.e.* shown in Fig. 6D. The improved kinetics of RhB could be due to its high affinity towards the membrane and the close interaction with the ROS produced by the composite α/β-Bi_2O_3 particles. Moreover, Fig. 6B shows no significant change in the RhB concentration in the case of treatment with the bare nylon membrane, under photolysis conditions.

3.2.3 Varied dye concentrations. To evaluate the membrane performance at high loading of the IC dye, the photocatalytic tests were conducted at varied IC concentrations using the Bi_2O_3/nylon composite. Fig. 6C and D show the C/C_o and removal kinetics of IC at concentrations of 5, 10 and 20 ppm, and reveal that the removal efficiency of the Bi_2O_3/nylon composite membrane decreased to 75.11% and 61.45% at concentrations of 10 and 20 ppm, respectively, during 180 minutes of irradiation exposure. This behavior could be related to the low availability/generation of ROS due to the attachment of the dye molecules on the active sites of α/β-Bi_2O_3. Secondly, the resulting increase in solution opacity and consequently the decreased irradiation transmission subsequently lowered the removal efficiency of IC.[60,61] Moreover, the high organic load could reduce the water flux and increase the mass transfer resistance of the membrane and could decrease the membrane efficiency.[62] This trend was observed during TOC analysis, which revealed a decrease in the degradation and mineralization efficiency of the composite membrane, *i.e.* after 180 min of irradiation, the analyzed TOC reduction was 63% and 37% for 10 and 20 ppm concentrations of IC dye, respectively, compared to 78% reduction in the case of 5 ppm solution. The resultant decrease in mineralization efficiency could be due to the saturation of the composite membrane with intermediate species that affected the semiconductor activation to support the generation of reactive species and induce oxidation. Fig. 6D shows calculated K_{app} values of 0.63×10^{-2} min^{-1} and 0.43×10^{-2} min^{-1} for 10 and 20 ppm IC dye concentrations, significantly reduced compared to 0.83×10^{-2} min^{-1} in the case of 5 ppm concentration.

3.2.4 Mixed dye degradation. Since colored wastewater contains mixtures of several dyes, interfering with each other in the mixed effluent, their removal behavior and mechanism of interaction for any potential treatment (including the case of membrane-assisted photocatalysis) could be different. Therefore, the evaluation of a mixed solution of both IC and RhB dyes was performed using the composite membrane. The recorded absorbance spectrum of the mixed solution *vs.* irradiation time given in Fig. 7A shows two main peaks corresponding to the contribution of both IC and RhB dyes at 610 and 555 nm, respectively. In Fig. 7B, the C/C_o profiles of the mixed solution at different times of photocatalytic exposure are reported *i.e.* using bare nylon and Bi_2O_3/nylon composite membranes.

Under dark conditions, both IC and RhB dyes preferentially adsorbed on the membrane at 23% and 22%, respectively. After irradiation, the absorbance of the IC dye was significantly reduced in the first 90 min (Fig. 7B), with the generated intermediate products absorbing in the UV region *i.e.* from 200 nm to 250 nm. Due to an intense peak (Fig. 7A), RhB dye depletion followed IC removal, but at slightly lower kinetics. Actually, the calculated K_{app} was 1.05×10^{-2} min^{-1} and 1.21×10^{-2} min^{-1} in the case of RhB and IC,

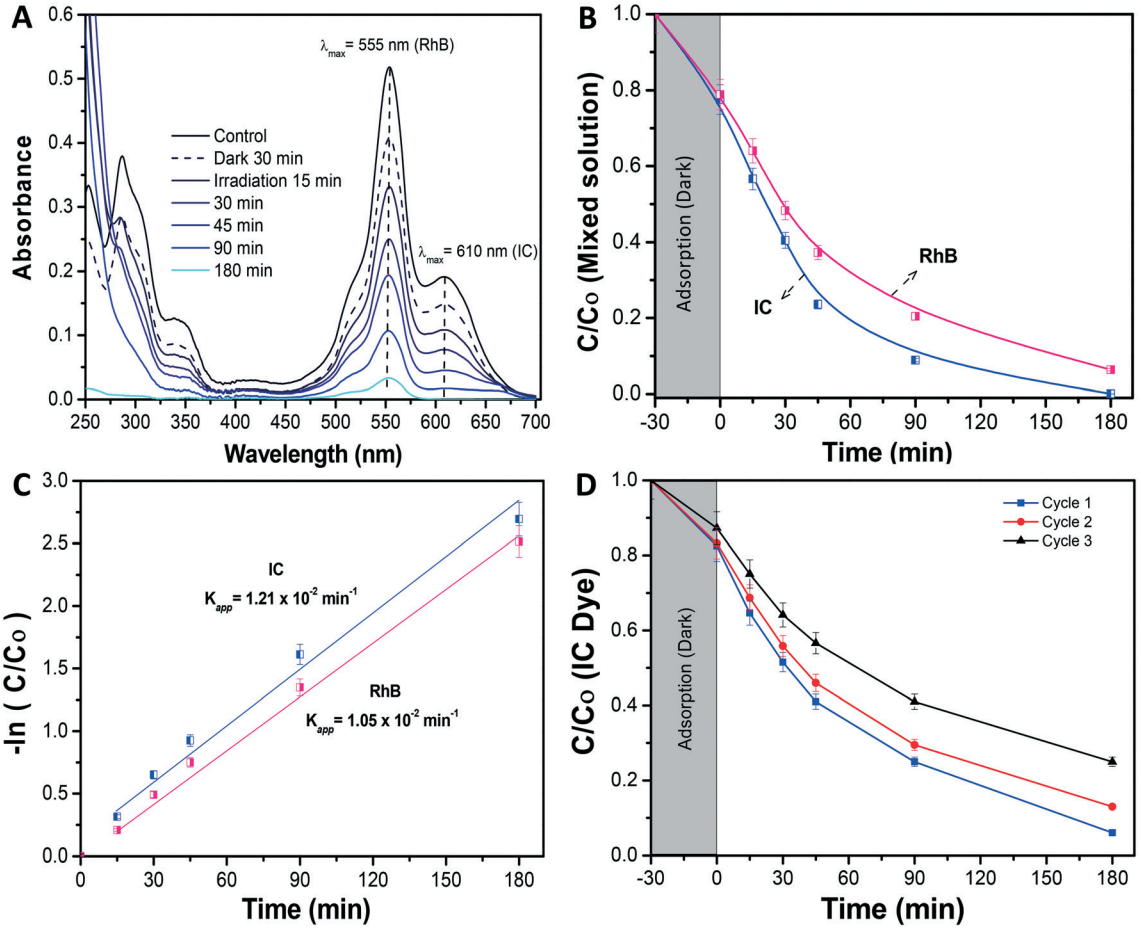

Fig. 7 A) Absorbance spectra *vs.* irradiation time of the mixed solution, B) relative concentration (C/C_o) of combined dyes degraded using the Bi_2O_3/nylon composite, C) kinetic curves of removal of IC and RhB dyes in the mixed solution, and estimated K_{app}, and D) cyclic stability of the Bi_2O_3/nylon composite membrane up to three cycles; C/C_o profiles at 5 ppm IC dye concentration.

respectively. The degradation kinetics of RhB was also found to be lower compared to when it was tested alone (K_{app} 1.57 × 10^{-2} min^{-1}) (Fig. 7C). This decrease in RhB removal kinetics probably was due to the limited ROS availability for the attack and degradation of both dyes. The investigation revealed that both dyes underwent simultaneous degradation with the formation of IC dye intermediate products probably because of the good interaction of both dyes enabled by the membrane, in contrast to our previously reported observation with the dispersed α/β-Bi_2O_3 nanoparticles, where IC was preferentially degraded, and after its complete degradation, the activity was directed against RhB.[42]

Here the equal and concurrent interaction of both dyes with the generated ROS is supported by the membrane. The overall obtained results suggested no/less interfering behavior among the tested dyes, as the removal kinetics of both dyes was almost similar *i.e.* from 1.21 × 10^{-2} min^{-1} and 1.05 × 10^{-2} min^{-1}, for IC and RhB, respectively.

3.2.5 Cyclic stability. For the cyclic stability of the Bi_2O_3/nylon nanocomposite membrane, the photocatalytic tests were carried out up to three cycles *i.e.* after the composite membrane was recovered, rinsed and configured again in the CPMR. Fig. 7D shows the relative concentration (C/C_o) decrease of the IC dye at 5 ppm concentration up to three cycles. The composite membrane showed good stability and performance in the first two cycles; however, the removal efficiency significantly decreased in the third cycle. This reduction could be associated with membrane exhaustion due to an altered porosity or to the affected active sites of the nylon fibers, and integrated α/β-Bi_2O_3 particles that previously had sustained the capture of dye molecules and intense interaction with the generated radical species.

3.3 Antibacterial activity

3.3.1 Bacterial inhibition in solid media. The main aim of this study was to evaluate the potential of the composite membrane for the photocatalytic inactivation of waterborne pathogens *i.e. E. coli*. Therefore, initially, the inhibition tests were performed on *E. coli* cultured in solid media. The obtained results, showed in Fig. 8A, confirmed a growth inhibition halo against *E. coli* in the case of the composite membrane compared to the bare nylon membrane and control samples (biotic control). The calculated zone of

inhibition was around 14 mm. Moreover, under dark conditions, no significant inhibition zone was observed in the case of the composite membrane, revealing that the integrated α/β-Bi_2O_3 particles remained inactive and did not generate ROS against the growth of *E. coli*. Only a little zone of inhibition was recorded in some replicates, highlighting that probably the integrated α/β-Bi_2O_3 particles at high concentration can be a little bit toxic against bacterial growth, too. Meanwhile in the case of bare nylon and control samples (without membranes), a high growth of *E. coli* was observed in the whole Petri dish, both under dark and irradiated conditions, resulting in no significant effect on bacterial growth.

3.3.2 Bacterial inhibition in a liquid suspension. Once the antibacterial activity of the composite membrane was assessed in solid agar media, the photocatalytic response against a liquid stock solution of *E. coli* at a concentration of 1×10^6 CFU mL^{-1} was evaluated by using the CPMR. The obtained results revealed a continuous *E. coli* reduction during the photocatalytic exposure *i.e.* as shown in Fig. 8B. The number of bacterial cells assessed by the plate count method of serially diluted samples collected from the CPMR at specified times confirmed the reduction of the cell density. It revealed 50% log reduction of *E. coli* after 90 min, and their complete removal after 240 min of treatment (as observed in Fig. 8B). To further confirm that the composite membrane has a biocidal effect on the microorganisms, fluorescence live/dead cell staining and imaging were applied *i.e.* using fluorescence microscopy. The samples were taken from the CPMR and stained, resulting in green-stained cells that represent living bacteria, whereas the red-stained cells are dead. The acquired fluorescence microscopy images of *E. coli* are shown in Fig. 9. In the beginning, plenty of live green-stained cells were observed, while at continued photocatalytic exposure, the red-stained cell increased their number. The obtained fluorescence images revealed that the bacterial cells were attacked by α/β-Bi_2O_3 in the composite membrane, resulting in the rupture of their cell membranes and allowing the PI dye to stain the DNA inside the nucleus, as indicated from the observed red-stained cells. After treatment of 240 min, the higher proportion of red-stained cells over green-stained cells revealed that the Bi_2O_3/nylon composite membrane has not only a biostatic effect (growth inhibition) on the treated *E. coli* cells, but it acts as a biocidal material, able to kill this bacterial strain. During the photocatalytic reaction, the catalytic material integrated into the membrane could produce ROS that could attack the bacterial cells, lead to cell damage, and increase the permeability of the cell membrane towards PI staining dye.[63] Compared to these results, the bare nylon and control samples showed no significant red stained (dead) cells after prolonged exposure; the acquired fluorescence images for bare nylon treatment and control (without any membrane) samples are given in ESI† Fig. S4.

3.4 Photocatalytic mechanism

The photocatalytic particles partially embedded in polymeric/ceramic membranes remained active under irradiation and released reactive oxidative species (ROS) in water media and across the adsorbed/retained pollutants.[61,64] The dispersion of ROS across the membrane could be affected by mass-transfer limitations. However, due to the large surface created by the multi-layered nylon membrane and the exposed appearance of α/β-Bi_2O_3 particles on these layers, the large release of ROS could have been enough to reach the nearest adsorbed/retained pollutants, resulting in dye degradation and bacterial inactivation, compared to bare nylon. Indeed, the obtained results suggest that the α/β-Bi_2O_3 nanocomposite membrane has good adsorption assisted photocatalytic properties against the removal of both anionic and cationic dyes as well as bacteria. Some of the reported studies suggested ROS generation around the surface of heterojunction α/β-Bi_2O_3 (ref. 42) and nanocomposite materials *i.e.* Sb_2WO_6/BiOBr and $BiSbO_4$/BiOBr.[38,39] In the case of dyes, there could be various possibilities of their interaction with the generated ROS on the α/β-Bi_2O_3 active sites of the composite membrane. Either the dye molecules

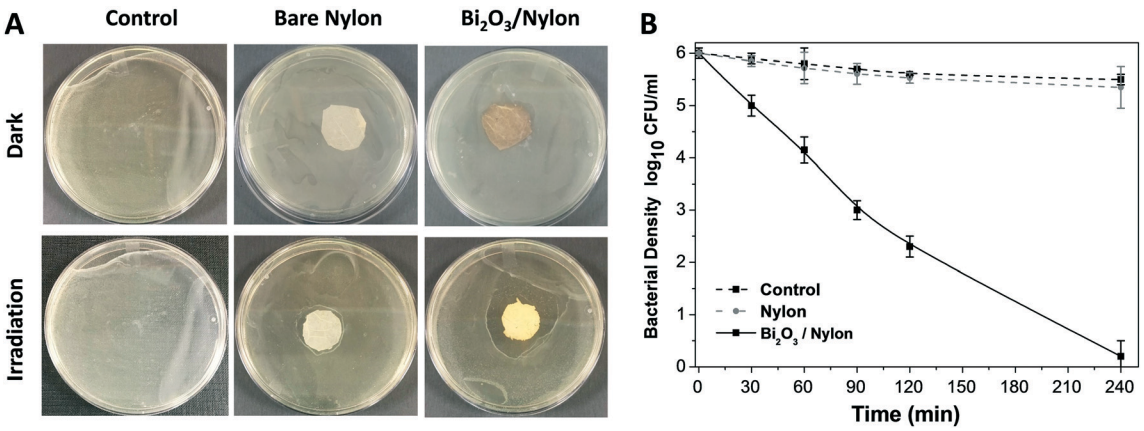

Fig. 8 A) Bacterial inhibition in solid media of control, bare nylon, and Bi_2O_3/nylon after incubation in the dark or under LED irradiation; B) *E. coli* density reduction in a liquid suspension treated with the photocatalytic Bi_2O_3/nylon membrane.

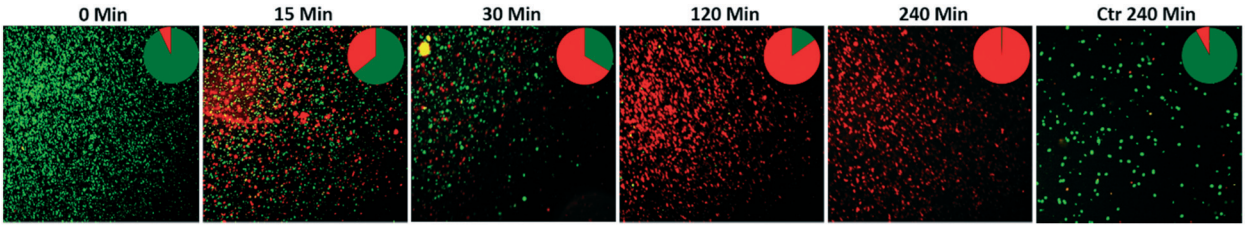

Fig. 9 Fluorescence stained images of live and dead *E. coli* cells at different treatment times.

of IC and RhB could have been adsorbed through ionic interaction *i.e.*, in the case of IC dye *via* sulphonic branched groups, while for RhB dye *via* the carboxylic group, or the dye molecules of IC and RhB were captured within the membrane pores of the multilayered nylon fibers. However, the good affinity of both dyes towards the composite membrane could be driven by both mechanisms *i.e.* through simultaneous ionic interaction and capture of dye molecules. After irradiation with visible light, the α/β-Bi_2O_3 particles in the composite membrane generated reactive species that attacked the captured/adsorbed dye molecules, performing adsorption-assisted photocatalysis. During the photo-discoloration of IC, the reactive species attacked the sulfonic groups, partially mineralized, and degraded into intermediate compounds identified as isatin sulfonic acid and 2-amine-5-sulfo-benzoic acid.[65] Meanwhile, the degradation of RhB followed the carboxylic acid oxidation and reduction path, being partly mineralized without any apparent shift of the absorbance in the UV-vis spectrum, typical of de-ethylation (see Fig. S3 in the ESI†).[42] In the case of the mixed solution, both dyes showed a good interaction and removal kinetics without any ionic inhibition/interference because of the equivalent interface provided by the membrane multilayers. Further, under prolonged exposure, the simultaneous degradation of both dyes occurred, due to the attack of ROS towards the IC and RhB dye molecules.

Concerning bacteria, the results obtained with *E. coli* revealed that probably the bacterial cells interacted with the composite α/β-Bi_2O_3 particles through multilayered channels, and were subsequently attacked by the generated ROS with resulting damage of the cell wall/membrane and their constituents. It is well-known that ROS can oxidise proteins, lipids and phospholipids,[66] damaging the membrane itself or simply its lipid bilayer organization, eventually leading to efflux of cytosolic contents or to cell lysis. These effects are particularly efficient on bacteria, fungi, and viruses, including multidrug-resistant strains, and due to their quick action, ROS are considered potent antimicrobial agents.[67] Similar mechanisms have been suggested for other antimicrobial metal and metal oxides, such as silver or copper, and are consistent with previous works that report the efficacy of β-Bi_2O_3 on *E. coli* and *S. aureus*.[68,69] The adsorption of the bacterial cells in the porous structure of the composite membrane combined with the action of the bismuth-based nanomaterial irradiated with LED visible light allowed a complete degradation of the pathogens. Indeed, the ROS generated by the photocatalytic action of the α/β-Bi_2O_3 activated particles are more effective in close vicinity, due to their extremely low half-life. The increased number of red-stained (dead) cells at increased photocatalytic exposure showed that live cells interacted with and were attacked continuously by the photo-originated ROS. All of these results proved the potential applicability of bismuth-based composite membranes for water treatment and sanitation.

4. Conclusion

An α/β-Bi_2O_3 powder semiconductor was synthesized by thermal annealing of $Bi(NO_3)_3{\cdot}5H_2O$ salt. The synthesized powder was integrated into the nylon-6 multilayered fibrous membrane *via* electrospraying, and characterized by XRD, FESEM, EDX, UV-vis, FT-IR and Raman analyses. The Bi_2O_3/nylon nanocomposite membrane showed a photocatalytic response against the separate solution of IC and RhB dyes, with a complete discoloration. The TOC analyses revealed the partial mineralization and degradation of IC and RhB treated solutions with the formation of stable and persistent intermediates. Further, in the case of the mixed solution of IC and RhB dyes, the composite membrane showed simultaneous degradation response to anionic IC dye and cationic RhB dye, due to their equal interaction with the reactive species, generated by α/β-Bi_2O_3. Moreover, dealing with a higher concentration of IC, the degradation kinetics was reduced by 3-fold, mainly due to the high saturation of the membrane layers by the dye-intermediates.

Furthermore, the composite membrane showed an antibacterial response against *E. coli* in solid and liquid cultures. In the case of solid *E. coli* media, the formation of a 14 mm inhibition zone was obtained, whereas, for the liquid *E. coli* suspension (1×10^6 CFU mL^{-1}), the complete inhibition of bacterial growth was attained after 240 min of photocatalytic exposure. The induced bactericidal effect on *E. coli* was observed by fluorescence microscopy which confirmed the high proportion of dead over live cells. Further, the successive recycle tests employing the used membrane suggested the suitable applications and efficacy of the Bi_2O_3/nylon nanocomposite membrane for the removal of organic dyes and inactivation of waterborne pathogens.

Conflicts of interest

There are no conflicts to declare.

Acknowledgements

The authors acknowledge the technical support of Prof. Zeeshan Khatri at the Mehran University of Engineering and Technology, Jamshoro, Pakistan, Prof. Jennifer Weidhaas at the University of Utah, USA, Dr. Paola Rivolo, and Dr. Pravin Jagdale from Politecnico di Torino, Italy, for their technical assistance. This study was financially supported by the United States Government and the American people through the United States Agency for International Development (USAID) and USPCAS-W, MUET research project funding. The contents are the sole responsibility of the authors and do not necessarily reflect the views of USAID or the United States Government.

References

1 S. C. A. Subramanian Seshadri, S. Ramachandran, K. Thirumavalavan and B. G. Prakash Kumar, A Review Of Solar Photocatalytic Degradation Of Wastewater Using Advanced Oxidation Processes, *J. Ind. Pollut. Control*, 2015, **31**(2), 297–309.

2 S. Natarajan, H. C. Bajaj and R. J. Tayade, Recent advances based on the synergetic effect of adsorption for removal of dyes from waste water using photocatalytic process, *J. Environ. Sci.*, 2018, **65**, 201–222.

3 H. Dong, G. Zeng, L. Tang, C. Fan, C. Zhang, X. He and Y. He, An overview on limitations of TiO_2-based particles for photocatalytic degradation of organic pollutants and the corresponding countermeasures, *Water Res.*, 2015, **79**, 128–146.

4 C. L. Bianchi, E. Colombo, S. Gatto, M. Stucchi, G. Cerrato, S. Morandi and V. Capucci, Photocatalytic degradation of dyes in water with micro-sized TiO_2 as powder or coated on porcelain-grès tiles, *J. Photochem. Photobiol., A*, 2014, **280**, 27–31.

5 T. A. Gadhi, L. S. Gómez-Velázquez, M. Bizarro, A. Hernández-Gordillo, A. Tagliaferro and S. E. Rodil, Evaluation of the photodiscoloration efficiency of β-Bi_2O_3 films deposited on different substrates by pneumatic spray pyrolysis, *Thin Solid Films*, 2017, **638**, 119–126.

6 C. Minero and D. Vione, A quantitative evalution of the photocatalytic performance of TiO_2 slurries, *Appl. Catal., B*, 2006, **67**, 257–269.

7 Y. Boyjoo, H. Sun, J. Liu, V. K. Pareek and S. Wang, A review on photocatalysis for air treatment: from catalyst development to reactor design, *Chem. Eng. J.*, 2017, **310**, 537–559.

8 K. Fujiwara, Y. Kuwahara, Y. Sumida and H. Yamashita, Fabrication of photocatalytic paper using TiO_2 nanoparticles confined in hollow silica capsules, *Langmuir*, 2017, **33**, 288–295.

9 G. R. M. Echavia, F. Matzusawa and N. Negishi, Photocatalytic degradation of organophosphate and phosphonoglycine pesticides using TiO_2 immobilized on silica gel, *Chemosphere*, 2009, **76**, 595–600.

10 T. Hirai, Y. Bando and I. Komasawa, Immobilization of CdS nanoparticles formed in reverse micelles onto alumina particles and their photocatalytic properties, *J. Phys. Chem. B*, 2002, **106**, 8967–8970.

11 B. Gao, P. S. Yap, T. M. Lim and T.-T. Lim, Adsorption-photocatalytic degradation of Acid Red 88 by supported TiO_2: Effect of activated carbon support and aqueous anions, *Chem. Eng. J.*, 2011, **171**, 1098–1107.

12 X. Wang, Y. Liu, Z. Hu, Y. Chen, W. Liu and G. Zhao, Degradation of methyl orange by composite photocatalysts nano-TiO_2 immobilized on activated carbons of different porosities, *J. Hazard. Mater.*, 2009, **169**, 1061–1067.

13 J. C. Joo, C. H. Ahn, D. G. Jang, Y. H. Yoon, J. K. Kim, L. Campos and H. Ahn, Photocatalytic degradation of trichloroethylene in aqueous phase using nano-ZNO/LAPONITE® composites, *J. Hazard. Mater.*, 2013, **263**, 569–574.

14 H. Khalilian, M. Behpour, V. Atouf and S. N. Hosseini, Immobilization of S, N-codoped TiO_2 nanoparticles on glass beads for photocatalytic degradation of methyl orange by fixed bed photoreactor under visible and sunlight irradiation, *Sol. Energy*, 2015, **112**, 239–245.

15 M. Borges, D. M. García, T. Hernández, J. C. Ruiz-Morales and P. Esparza, Supported photocatalyst for removal of emerging contaminants from wastewater in a continuous packed-bed photoreactor configuration, *Catalysts*, 2015, **5**, 77–87.

16 A. S. El-Kalliny, S. F. Ahmed, L. C. Rietveld and P. W. Appel, Immobilized photocatalyst on stainless steel woven meshes assuring efficient light distribution in a solar reactor, *Drinking Water Eng. Sci.*, 2014, **7**, 41–52.

17 D. Pérez-Mezcua, I. Bretos, R. Jiménez, J. Ricote, R. J. Jiménez-Rioboó, C. G. Da Silva, D. Chateigner, L. Fuentes-Cobas, R. Sirera and M. L. Calzada, Photochemical solution processing of films of metastable phases for flexible devices: the β-Bi_2O_3 polymorph, *Sci. Rep.*, 2016, **6**, 39561.

18 H. Dong, G. Zeng, L. Tang, C. Fan, C. Zhang, X. He and Y. He, An overview on limitations of TiO_2-based particles for photocatalytic degradation of organic pollutants and the corresponding countermeasures, *Water Res.*, 2015, **79**, 128–146.

19 U. I. Gaya and A. H. Abdullah, Heterogeneous photocatalytic degradation of organic contaminants over titanium dioxide: A review of fundamentals, progress and problems, *J. Photochem. Photobiol., C*, 2008, **9**, 1–12.

20 J. M. Arsuaga, A. Sotto, G. del Rosario, A. Martínez, S. Molina, S. B. Teli and J. de Abajo, Influence of the type, size, and distribution of metal oxide particles on the properties of nanocomposite ultrafiltration membranes, *J. Membr. Sci.*, 2013, **428**, 131–141.

21 J. García-Ivars, M.-J. Corbatón-Báguena and M.-I. Iborra-Clar, Development of mixed matrix membranes: Incorporation of metal nanoparticles in polymeric membranes, in *Nanoscale Materials in Water Purification*, Elsevier, 2019, pp. 153–178.

22 Z. Xu, T. Wu, J. Shi, K. Teng, W. Wang, M. Ma, J. Li, X. Qian, C. Li and J. Fan, Photocatalytic antifouling PVDF ultrafiltration membranes based on synergy of graphene oxide and TiO_2 for water treatment, *J. Membr. Sci.*, 2016, **520**, 281–293.

23 H. Ngang, B. Ooi, A. Ahmad and S. Lai, Preparation of PVDF–TiO_2 mixed-matrix membrane and its evaluation on dye adsorption and UV-cleaning properties, *Chem. Eng. J.*, 2012, **197**, 359–367.
24 P. Argurio, E. Fontananova, R. Molinari and E. Drioli, Photocatalytic membranes in photocatalytic membrane reactors, *Processes*, 2018, **6**, 162.
25 K. Zarrini, A. A. Rahimi, F. Alihosseini and H. Fashandi, Highly efficient dye adsorbent based on polyaniline-coated nylon-6 nanofibers, *J. Cleaner Prod.*, 2017, **142**, 3645–3654.
26 U. A. Qureshi, Z. Khatri, F. Ahmed, A. S. Ibupoto, M. Khatri, F. K. Mahar, R. Z. Brohi and I. S. Kim, Highly efficient and robust electrospun nanofibers for selective removal of acid dye, *J. Mol. Liq.*, 2017, **244**, 478–488.
27 H. R. Pant, M. P. Bajgai, K. T. Nam, Y. A. Seo, D. R. Pandeya, S. T. Hong and H. Y. Kim, Electrospun nylon-6 spider-net like nanofiber mat containing TiO_2 nanoparticles: a multifunctional nanocomposite textile material, *J. Hazard. Mater.*, 2011, **185**, 124–130.
28 N. Beyth, Y. Houri-Haddad, A. Domb, W. Khan and R. Hazan, Alternative Antimicrobial Approach: Nano-Antimicrobial Materials, *J. Evidence-Based Complementary Altern. Med.*, 2015, **2015**, 246012.
29 L. Y. Ng, A. W. Mohammad, C. P. Leo and N. Hilal, Polymeric membranes incorporated with metal/metal oxide nanoparticles: a comprehensive review, *Desalination*, 2013, **308**, 15–33.
30 S. R. Lakhotia, M. Mukhopadhyay and P. Kumari, Cerium oxide nanoparticles embedded thin-film nanocomposite nanofiltration membrane for water treatment, *Sci. Rep.*, 2018, **8**, 1–10.
31 J. Wang, W. Liu, H. Li, H. Wang, Z. Wang, W. Zhou and H. Liu, Preparation of cellulose fiber–TiO_2 nanobelt–silver nanoparticle hierarchically structured hybrid paper and its photocatalytic and antibacterial properties, *Chem. Eng. J.*, 2013, **228**, 272–280.
32 A. F. de Faria, A. C. M. de Moraes, P. F. Andrade, D. S. da Silva, M. do Carmo Gonçalves and O. L. Alves, Cellulose acetate membrane embedded with graphene oxide-silver nanocomposites and its ability to suppress microbial proliferation, *Cellulose*, 2017, **24**, 781–796.
33 M. Zahid, E. L. Papadopoulou, G. Suarato, V. D. Binas, G. Kiriakidis, I. Gounaki, O. Moira, D. Venieri, I. S. Bayer and A. Athanassiou, Fabrication of visible light-induced antibacterial and self-cleaning cotton fabrics using manganese doped TiO_2 nanoparticles, *ACS Appl. Bio Mater.*, 2018, **1**, 1154–1164.
34 M. Ou, S. Wan, Q. Zhong, S. Zhang, Y. Song, L. Guo, W. Cai and Y. Xu, Hierarchical Z-scheme photocatalyst of g-C_3N_4@Ag/$BiVO_4$ (040) with enhanced visible-light-induced photocatalytic oxidation performance, *Appl. Catal., B*, 2018, **221**, 97–107.
35 Z. Ai, Y. Huang, S. Lee and L. Zhang, Monoclinic α-Bi_2O_3 photocatalyst for efficient removal of gaseous NO and HCHO under visible light irradiation, *J. Alloys Compd.*, 2011, **509**, 2044–2049.
36 Y. Sun, W. Wang, L. Zhang and Z. Zhang, Design and controllable synthesis of α–/γ-Bi_2O_3 homojunction with synergetic effect on photocatalytic activity, *Chem. Eng. J.*, 2012, **211**, 161–167.
37 M. Jia, X. Hu, S. Wang, Y. Huang and L. Song, Photocatalytic properties of hierarchical BiOXs obtained via an ethanol-assisted solvothermal process, *J. Environ. Sci.*, 2015, **35**, 172–180.
38 Y. Wang, K. Wang, J. Wang, X. Wu and G. Zhang, Sb_2WO_6/BiOBr 2D nanocomposite S-scheme photocatalyst for NO removal, *J. Mater. Sci. Technol.*, 2020, **56**, 236–243.
39 Z. Wang, K. Wang, Y. Li, L. Jiang and G. Zhang, Novel $BiSbO_4$/BiOBr nanoarchitecture with enhanced visible-light driven photocatalytic performance: oxygen-induced pathway of activation and mechanism unveiling, *Appl. Surf. Sci.*, 2019, **498**, 143850.
40 S. Sood, A. Umar, S. K. Mehta and S. K. Kansal, α-Bi_2O_3 nanorods: an efficient sunlight active photocatalyst for degradation of Rhodamine B and 2,4,6-trichlorophenol, *Ceram. Int.*, 2015, **41**, 3355–3364.
41 X. Meng and Z. Zhang, Bismuth-based photocatalytic semiconductors: introduction, challenges and possible approaches, *J. Mol. Catal. A: Chem.*, 2016, **423**, 533–549.
42 T. A. Gadhi, A. Hernández-Gordillo, M. Bizarro, P. Jagdale, A. Tagliaferro and S. E. Rodil, Efficient α/β-Bi_2O_3 composite for the sequential photodegradation of two-dyes mixture, *Ceram. Int.*, 2016, **42**, 13065–13073.
43 M. H. El-Newehy, S. S. Al-Deyab, E.-R. Kenawy and A. Abdel-Megeed, Nanospider Technology for the Production of Nylon-6 Nanofibers for Biomedical Applications, *J. Nanomater.*, 2011, **2011**, 626589.
44 A. Hernández-Gordillo, M. Bizarro, T. A. Gadhi, A. Martínez, A. Tagliaferro and S. E. Rodil, Good practices for reporting the photocatalytic evaluation of a visible-light active semiconductor: Bi_2O_3, a case study, *Catal. Sci. Technol.*, 2019, **9**, 1476–1496.
45 J.-A. Park, K. Y. Cho, C. H. Han, A. Nam, J.-H. Kim, S.-H. Lee and J.-W. Choi, Quaternized Amphiphilic Block Copolymers/Graphene Oxide and a Poly (vinyl alcohol) Coating Layer on Graphene Oxide/Poly (vinylidene fluoride) Electrospun Nanofibers for Superhydrophilic and Antibacterial Properties, *Sci. Rep.*, 2019, **9**, 1–13.
46 A. Chiadò, L. Varani, F. Bosco and L. Marmo, Opening study on the development of a new biosensor for metal toxicity based on Pseudomonas fluorescens pyoverdine, *Biosensors*, 2013, **3**, 385–399.
47 B. Tomšič, B. Simončič, B. Orel, M. Žerjav, H. Schroers, A. Simončič and Z. Samardžija, Antimicrobial activity of AgCl embedded in a silica matrix on cotton fabric, *Carbohydr. Polym.*, 2009, **75**, 618–626.
48 N. Murthy and H. Minor, Analysis of poorly crystallized polymers using resolution enhanced X-ray diffraction scans, *Polymer*, 1995, **36**, 2499–2504.
49 T. J. Athauda, U. Butt and R. R. Ozer, Hydrothermal growth of ZnO nanorods on electrospun polyamide nanofibers, *MRS Commun.*, 2013, **3**, 51.

50 Y. Yu, R. Ma, S. Yan and J. Fang, Preparation of multi-layer nylon-6 nanofibrous membranes by electrospinning and hot pressing methods for dye filtration, *RSC Adv.*, 2018, **8**, 12173–12178.

51 K.-H. Lee, K.-W. Kim, A. Pesapane, H.-Y. Kim and J. F. Rabolt, Polarized FT-IR study of macroscopically oriented electrospun nylon-6 nanofibers, *Macromolecules*, 2008, **41**, 1494–1498.

52 E. Fatarella, D. Spinelli, M. Ruzzante and R. Pogni, Nylon 6 film and nanofiber carriers: Preparation and laccase immobilization performance, *J. Mol. Catal. B: Enzym.*, 2014, **102**, 41–47.

53 F. He, Z. He, J. Xie and Y. Li, IR and Raman spectra properties of Bi_2O_3-ZnO-B_2O_3-BaO quaternary glass system, *Am. J. Anal. Chem.*, 2014, **5**, 1142.

54 A. Milani, Unpolarized and polarized Raman spectroscopy of nylon-6 polymorphs: a quantum chemical approach, *J. Phys. Chem. B*, 2015, **119**, 3868–3874.

55 C. Menchaca, B. Manoun, G. Martínez-Barrera, V. Castaño and H. López-Valdivia, In situ high-temperature Raman study of crystalline nylon 6, 12 fibers gamma-irradiated in argon atmosphere, *J. Phys. Chem. Solids*, 2006, **67**, 2111–2118.

56 C.-H. Ho, C.-H. Chan, Y.-S. Huang, L.-C. Tien and L.-C. Chao, The study of optical band edge property of bismuth oxide nanowires α-Bi_2O_3, *Opt. Express*, 2013, **21**, 11965–11972.

57 A. L. Pereira, J. A. Sans, R. Vilaplana, O. Gomis, F. Manjón, P. Rodriguez-Hernandez, A. Muñoz, C. Popescu and A. Beltrán, Isostructural second-order phase transition of β-Bi_2O_3 at high pressures: an experimental and theoretical study, *J. Phys. Chem. C*, 2014, **118**, 23189–23201.

58 M.-W. Kim, B. Joshi, E. Samuel, K. Kim, Y.-I. Kim, T.-G. Kim, M. T. Swihart and S. S. Yoon, Highly nanotextured β-Bi_2O_3 pillars by electrostatic spray deposition as photoanodes for solar water splitting, *J. Alloys Compd.*, 2018, **764**, 881–889.

59 M. Ghani, A. A. Gharehaghaji, M. Arami, N. Takhtkuse and B. Rezaei, Fabrication of Electrospun Polyamide-6/Chitosan Nanofibrous Membrane toward Anionic Dyes Removal, *J. Nanotechnol.*, 2014, **2014**, 278418.

60 L. Aoudjit, P. M. Martins, F. Madjene, D. Petrovykh and S. Lanceros-Mendez, Photocatalytic reusable membranes for the effective degradation of tartrazine with a solar photoreactor, *J. Hazard. Mater.*, 2018, **344**, 408–416.

61 X. Zheng, Z.-P. Shen, L. Shi, R. Cheng and D.-H. Yuan, Photocatalytic membrane reactors (PMRs) in water treatment: configurations and influencing factors, *Catalysts*, 2017, **7**, 224.

62 R. Halim, R. Utama, S. Cox and P. Le-Clech, Performances of submerged membrane photocatalysis reactor during treatment of humic substances, *Membr. Water Treat.*, 2010, **1**, 283–296.

63 A. Mecha, M. Onyango, A. Ochieng and M. Momba, UV and solar photocatalytic disinfection of municipal wastewater: inactivation, reactivation and regrowth of bacterial pathogens, *Int. J. Environ. Sci. Technol.*, 2019, **16**, 3687–3696.

64 V. Melinte, L. Stroea and A. L. Chibac-Scutaru, Polymer Nanocomposites for Photocatalytic Applications, *Catalysts*, 2019, **9**, 986.

65 T. T. Guaraldo, T. B. Zanoni, S. I. de Torresi, V. R. Gonçales, G. J. Zocolo, D. P. Oliveira and M. V. B. Zanoni, On the application of nanostructured electrodes prepared by Ti/TiO_2/WO_3 "template": A case study of removing toxicity of indigo using visible irradiation, *Chemosphere*, 2013, **91**, 586–593.

66 M. Y. Memar, R. Ghotaslou, M. Samiei and K. Adibkia, Antimicrobial use of reactive oxygen therapy: current insights, *Infect. Drug Resist.*, 2018, **11**, 567.

67 M. Dryden, Reactive oxygen species: a novel antimicrobial, *Int. J. Antimicrob. Agents*, 2018, **51**, 299–303.

68 Y.-G. Yuan, Q.-L. Peng and S. Gurunathan, Effects of silver nanoparticles on multiple drug-resistant strains of Staphylococcus aureus and *Pseudomonas aeruginosa* from mastitis-infected goats: an alternative approach for antimicrobial therapy, *Int. J. Mol. Sci.*, 2017, **18**, 569.

69 M. K. Ballo, S. Rtimi, S. Mancini, J. Kiwi, C. Pulgarin, J. M. Entenza and A. Bizzini, Bactericidal activity and mechanism of action of copper-sputtered flexible surfaces against multidrug-resistant pathogens, *Appl. Microbiol. Biotechnol.*, 2016, **100**, 5945–5953.